Deep Dynamic Stall and Active Aerodynamic Modification on a S833 Airfoil using Pitching Trailing Edge Flap

Farid Samara[1] and David A. Johnson[2]

Abstract

Due to the dynamic nature of the wind resource, wind turbine blades are subjected to significant variation in flow parameters such as angle of attack (α). In some cases, the occurrence of dynamic stall on wind turbine blades causes load fluctuation which leads to material fatigue that tend to decrease the lifespan of the blades. In this study, the influence of a trailing edge flap (TEF) on dynamic stall effects is investigated at high α typical of wind turbines but atypical elsewhere. Pitching of the TEF was found to have a significant impact on the dynamic stall hysteresis loops responsible for the load fluctuation. Frequency analysis showed that the TEF was capable of reducing the cyclic fluctuation in the coefficient of lift and root bending moment by at least 26% and 24% respectively. These results are a significant contribution towards understanding the advantages of using TEFs and how implementing them will reduce wind turbine blade load fluctuations.

Introduction

Wind energy, an established renewable source of energy, has evolved over the last several decades to produce a significant share of electricity generation across the world. The success of horizontal axis wind turbines (HAWT) is due to innovation that has decreased the electricity production cost per kWh (Dykes et al., 2019). It is understood that most wind turbines spend most of the time in a relatively unsteady flow environment caused by many factors including wind shear, rotor misalignment, and turbulence of the wind resource to name a few (Shipley et al., 1995; Leishman, 2006). This flow unsteadiness causes cyclic loading on the blades that leads to material fatigue which decreases the lifespan of the blades. Fatigue life governs the design factors for larger wind turbines, so it is important to minimize the cyclic loading (Barlas and van Kuik, 2010). For this reason, it is imperative to understand and reduce cyclic loading on the blades to increase turbine lifespan and decrease the cost of generated energy. **To reduce cyclic loading and material fatigue, active aerodynamic modification of the blade, also known as *Smart Rotor*, could be used. Different active aerodynamic control strategies have been summarized and reviewed by Barlas and van Kuik (2010). They found that trailing edge flaps (TEFs) were the most efficient of the control strategies tested because of their control authority over the coefficients of lift and drag, linearity, high frequency response and simplicity of use. A TEF is achieved by hinging the trailing edge of the airfoil at a specific location.**

Cyclic loading on a rotating turbine blade tends to be caused by a variation in the blade local angle of attack, α, and that variation is due to the unsteady flow environment mentioned. In some

[1]Ph.D., Wind Energy Group, Mechanical and Mechatronics Engineering, University of Waterloo, Waterloo, Canada; fsamara@uwaterloo.ca
[2]Professor, Wind Energy Group, Mechanical and Mechatronics Engineering, University of Waterloo, Waterloo, Canada; david.johnson@uwaterloo.ca

Corresponding author:
Farid Samara, Wind Energy Group, Mechanical and Mechatronics Engineering, University of Waterloo, 200 University Ave W, Waterloo, Canada N2L 3G1
Email: fsamara@uwaterloo.ca

Nomenclature

α	angle of attack, deg		C_M	coefficient of moment, [-]
α_{amp}	pitching semi-amplitude, deg		C_p	coefficient of pressure, [-]
α_F	flap angle of attack, deg		f	frequency of oscillation, s^{-1}
$\alpha_{mean,F}$	flap pitching mean geometric angle of attack, deg		f_F	flap frequency of oscillation, s^{-1}
			f_p	pitch frequency of oscillation, s^{-1}
α_{mean}	pitching mean geometric angle of attack, deg		k	reduced frequency ($k = \pi c f / U_\infty$)
γ	yaw angle, deg		U_∞	free stream velocity, m.s^{-1}
ϕ	phase shift, rad		c	chord, m
ρ_∞	free stream air density, kg.m^{-3}		cw	clockwise
τ	period of the cycle, s		cww	counter-clockwise
C_D	coefficient of drag, [-]		PSD	Power Spectral Density
C_L	coefficient of Lift, [-]		STD	standard deviation

cases, for example when the turbine is yawed, the α variation tends to be cyclic in nature with a frequency of once per rotor revolution (Burton et al., 2011). This cyclic variation in α not only causes load variation based on steady flow dynamics but also on unsteady flow dynamics or dynamic stall under specific conditions. A 2D airfoil undergoing pitching in a wind tunnel could be used to study and simulate dynamic stall. In this experimental campaign, the use of a TEF on a pitching airfoil is investigated to reduce cyclic loading that could be caused by the occurrence of dynamic stall on the blade. It is then important to understand the characteristics and formation of dynamic stall in this application.

When the airfoil pitching range exceeds the static stall angle by a few degrees, then dynamic stall ensues according to McCroskey (1982). Dynamic stall is characterized by extreme hysteresis and non-linear cycles in the coefficient of lift (C_L), coefficient of moment (C_M) and coefficient of drag (C_D) (McCroskey, 1982). The dynamic stall cycle could be divided into four sections as seen in Figure 1: a) start of pitch-up motion, b) flow separation, c) start of pitch-down motion, and d) flow reattachment. During pitch-up motion, as C_L increases steadily past the static stall angle, there is a sudden spike in C_L caused by the formation of a leading edge vortex (LEV) also known as the dynamic stall vortex (Corke and Thomas, 2015) shown in Figure 1. The LEV is generated at the leading edge (LE) and convects downstream along the airfoil towards the trailing edge (TE). The LEV generation and convection produces values of C_L, C_M and C_D that are much higher than their static counterparts (McCroskey, 1982). After the LEV flows past the TE the flow separates leading to a severe loss in lift, an increase in nose-down pitching moment and an increase in drag. In some cases a secondary LEV is formed and shed, leading to another C_L peak (Leishman, 1990). Gharali and Johnson (2013, 2015) and Gharali et al. (2015) reported the formation of a secondary LEV and in some cases smaller vortices after that. The secondary LEV tends to be weaker in magnitude when compared to the primary LEV. Lee and Gerontakos (2004) have also reported the formation of a secondary LEV. Typically, during pitch-down motion, the airfoil is stalled even when α is below the static stall angle. The flow then reattaches to the surface as α decreases and the cycle starts again (Baik et al., 2012; Cebeci et al., 2005; Pitt Ford and Babinsky, 2013). Leishman (1990) and recently Masdari et al. (2018) studied the effects of mean α, pitching amplitude, and reduced frequency on dynamic stall. Surface pressure measurements have been used in the past to determine the formation and development of dynamic stall and the LEV by Leishman (1990), McCroskey et al. (1976) and others. These studies show how the LEV could be identified using surface pressure measurements alone.

While the airfoil is pitching past the static stall angle and dynamic stall is present, aeroelastic stability problems could arise. Aeroelastic divergence or stall flutter is promoted when torsional damping (defined by the line integral $\oint C_m(\alpha)d\alpha$) is negative (Leishman, 2006). A counter-clockwise (ccw) loop in the $C_M - \alpha$ plot indicates that the torsional damping is positive while a clockwise (cw) loop indicates that the torsional damping is negative. Negative
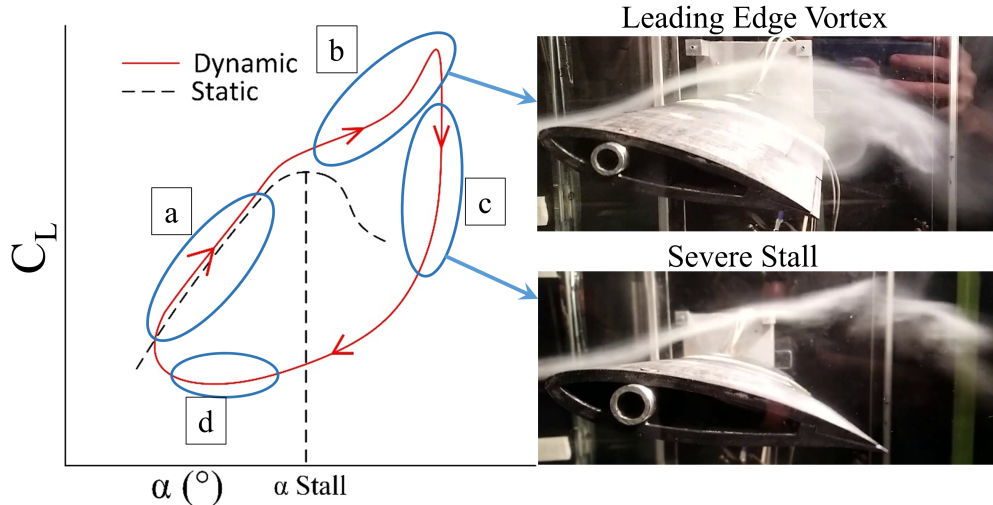
Figure 1. A schematic illustrating the influence of the dynamic stall cycle on the airfoil C_L. The cycle is divided into four sections: a) start of pitch-up motion, b) flow separation, c) start of pitch-down motion and d) flow re-attachment. The pictures, taken during the experimental campaign, help visualize the LEV re-circulation and stall.

damping may lead to structural vibrations and rapid mechanical failure if the structural dynamics permit (Corke and Thomas, 2015; Green et al., 2011). Using a TEF to mitigate negative damping without significant loss of lift would benefit the energy capture and turbine system greatly and would ensure limited flutter on the airfoil (Green et al., 2011).

TEF also known as plain flap, or aileron has been used in the past in the aviation industry to modify the aerodynamic characteristics and obtain higher C_L values (Abbott and Doenhoff, 1959). A plain flap is described to be a relatively crude device and is likely to lead to some form of boundary layer separation (Houghton and Carpenter, 2002). This means that there is always a possibility of partial separation when the flap is deflected. Abbott and Greenberg (1939) studied a plain flap of 20% chord on a static NACA 23012 airfoil with a large range of flap and pitch angles. They found that the TEF was capable of shifting the entire $C_L - \alpha$ data up and down in both pre-stall and stall flow equally. The stall angle was also shifted slightly to a lower or higher angle depending on the flap position. The flap not only has influence over C_L, but also has a large impact on C_M and C_D. Their results showed that a positive flap angle, defined in this paper as deflection towards the suction side (See Figure 4), increased C_D significantly but a negative flap angle only had a slight impact on C_D. Jacobs and Pinkerton (1931) showed that the TEF changes the static surface pressure distribution not only at the TE but at the LE as well. Most of the prior research regarding flaps is focused on negative flap angles to achieve higher C_L values of relevance to the aviation industry. When applying flaps on wind turbines it is as important to equally understand the aerodynamics of the airfoil in positive and negative flap angles alike to reduce the cyclic loading on the airfoil. The Static Airfoil Characterization section of this paper focuses on understanding how large flap angles (higher than $\pm 20°$) influence the aerodynamics of a wind turbine airfoil in static conditions.

In recent years, TEFs have been investigated and used to manipulate or reduce the impact of dynamic stall on airfoils. In most cases, the TEF would be oscillating at a frequency equal to that of the airfoil pitching frequency but with a phase shift defined as ϕ that influences the shape of the dynamic stall loops. Having the appropriate ϕ is key to reducing the load fluctuation due to dynamic stall. Choosing the appropriate ϕ is dependent on the oscillating dynamics such as the mean α, pitching amplitude, and reduced frequency. Lee and Gerontakos (2006); Lee and Su (2011) investigated how a TEF can influence the formation and detachment of LEV. They concluded that the TEF was not capable of controlling the formation and detachment of the LEV but was capable of controlling the LEV magnitude. Green et al. (2011) discuss the benefit of TEF and how it can influence dynamic stall behavior. They reported that flap deflection was capable of reducing the hysteresis cycle in the lift and moment data. **Furthermore, with the appropriate ϕ, negative torsional damping could be reduced or completely eliminated.** Raiola et al. (2018) showed that a TEF on a NACA0015 airfoil was capable of controlling the loads generated by dynamic stall and the LEV. Troldborg (2005) was able to use the TEF motion to counteract the oscillating pitch motion and obtain smooth lift data on

the airfoil. Zanotti and Gibertini (2018) investigated the use of an active Gurney flap for dynamic stall control on a pitching airfoil and found that the flap was capable of reducing the amplitude of dynamic stall. Feszty et al. (2004) and Shehata et al. (2018) showed that pulsing the TEF was capable of improving wind turbine rotor performance and removing negative effects of dynamic stall. From the literature review presented, it was found that more data is needed regarding dynamic stall behavior on wind turbine specific airfoils and cambered airfoils with a TEF.

In some operating conditions, a percentage of the wind turbine blade span could be experiencing α values higher than 30°. Gallant and Johnson (2017) measured α on a wind turbine blade operating under yaw conditions to be oscillating around a mean α of 25° with an amplitude of 5°. Most of the papers and references presented so far study the dynamic stall cycle where the maximum pitch angle is 25°. In this current paper, deep dynamic stall is investigated on a cambered airfoil with a TEF where the maximum pitch angle reaches 30° while the airfoil is oscillating. Few studies investigate deep dynamic stall on an airfoil and present data for pitch angles past 25° (Leishman, 1990; McCroskey, 1981; Gerontakos, 2004; Zanotti, 2012; Zanotti and Gibertini, 2013). The literature was found to lack data on a cambered airfoil equipped with a TEF and operating in deep stall. This paper builds on prior studies and specifically discusses the S833 cambered airfoil that was designed for small scale wind turbines (Somers, 2005). An experimental campaign was initiated to study a TEF on a wind turbine beginning with characterizing a 2D airfoil model with a TEF in a closed loop wind tunnel at a chord $Re= 170 \times 10^3$ and a reduced frequency (k) of 0.06 and 0.1. Time resolved surface pressure measurements on the airfoil element have been obtained for different dynamic cases and flap positions. A few of the novel contributions introduced in this paper are: the design and actuation of a TEF on a small airfoil section, and dynamic stall studies on a wind turbine specific airfoil in deep dynamic stall cases with an oscillating TEF.

Experimental Setup

First, the instrumented airfoil model is explained briefly along with the wind tunnel setup. Secondly, the airfoil motion and different test cases are presented. Finally, the validation for the differential pressure measurement technique is discussed.

Wind Tunnel Setup

The experimental campaign was carried out in the closed loop wind tunnel at the University of Waterloo. The wind tunnel has a contraction ratio of 9:1 and a cross section of 0.61 m square. The uniformity was found to be within $\pm$ 0.4% in the spanwise and vertical direction. The turbulence intensity was 0.1%. The free-stream velocity was set by the static pressure drop across the contraction with an uncertainty of less than 2.5%. The blockage ratio was around 8%. The wind tunnel velocity or the free stream velocity, U_∞, was set to 15 m/s resulting in a chord-based Reynolds number (Re) of 170×10^3. This velocity was based upon a compromise between high Reynolds number and an achievable pitch frequency to achieve dynamic stall behavior on the airfoil.

The NREL S833 airfoil (Somers, 2005), designed for small wind turbines, was used for the experiments. The flap width was chosen to be 20% of the 178 mm model chord. **The flap span was not capable of occupying the entire model span due to geometric restrictions including bearings and flap motor. Thus, the flap span occupied 60% of the 584 mm model span**. To incorporate the sensors and actuators the aerodynamic airfoil segment was 3D printed. A stainless steel spar at the quarter chord was used to support the 3D printed airfoil segments and hold all the components together. The airfoil was then cantilevered and supported on the motor drive side in the wind tunnel. Two strain gage groups were used to measure the strain at the airfoil support to study the load on the entire airfoil section. Precision strain gages (Omega SGD-7/100 0-DY11) were calibrated and connected in a full-bridge configuration to increase sensitivity and reduce temperature dependence. A schematic of the experimental setup is shown in Figure 2. The designed model was capable of housing the TEF actuator and controller inside the airfoil. The airfoil internal arrangement of the flap motion control could be seen in Figure 3.

To determine the coefficient of lift and moment, the phase-averaged pressure was integrated from the 54 surface pressure taps located on an aluminum airfoil section at midspan with 4 of those pressure taps located on the flap. The aluminum pressure tap section was placed at the center of the wind tunnel section sandwiched between the 3D printed airfoil pieces. To measure the surface pressure, 27 differential pressure transducers (All Sensors model 120 cmH2O-D1-4V-MINI) were used to measure the differential pressure between the suction and pressure side of the airfoil at the same chordwise location simultaneously. **This technique was successfully used by Raiola et al. (2018) on a symmetric airfoil. To validate this technique so it could be used on cambered airfoils, Samara and Johnson (2020a) conducted a set of experiments to compare differential pressure measurements**
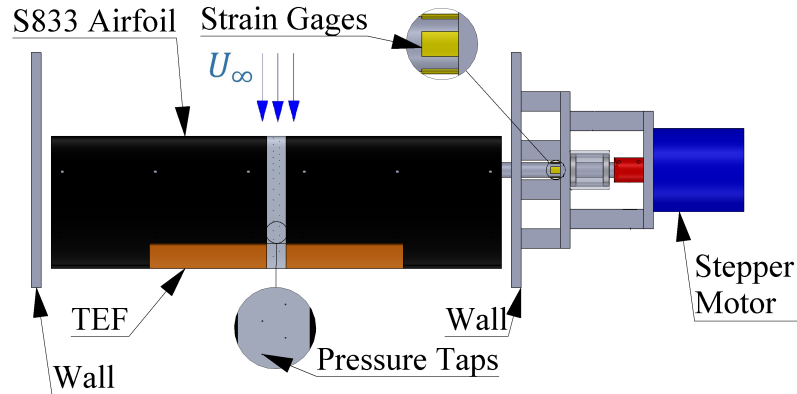
Figure 2. A plan view schematic showing how the airfoil was setup inside the wind tunnel for characterization.

to single ended pressure measurements. They concluded that both techniques are valid to study the patterns in C_L and C_M on cambered airfoils and the maximum error between both techniques is less than 4%. The 3D printed airfoil model was capable of housing the pressure transducers and all the tubing needed to connect the transducers to the pressure taps. Refer to Figure 3 for more clarification. The coefficient of pressure (ΔC_p) is calculated as $\Delta C_p = (p_{suction\ side} - p_{pressure\ side})/(\frac{1}{2}\rho_\infty U_\infty^2)$ where ρ_∞ is the free stream fluid density. The average representative uncertainty in C_L or C_M was calculated to be ± 0.069 and ± 0.014 respectively. Uncertainty in ΔC_p was calculated to be around 0.085. The uncertainty was based on the error in the pressure transducers and wind tunnel velocity. The uncertainty in α and TEF angle is $\pm 0.1°$ and $\pm 2°$ respectively. More details regarding the experimental setup could be found in Samara and Johnson ((Samara and Johnson, 2018, 2020b; Samara, 2020)).
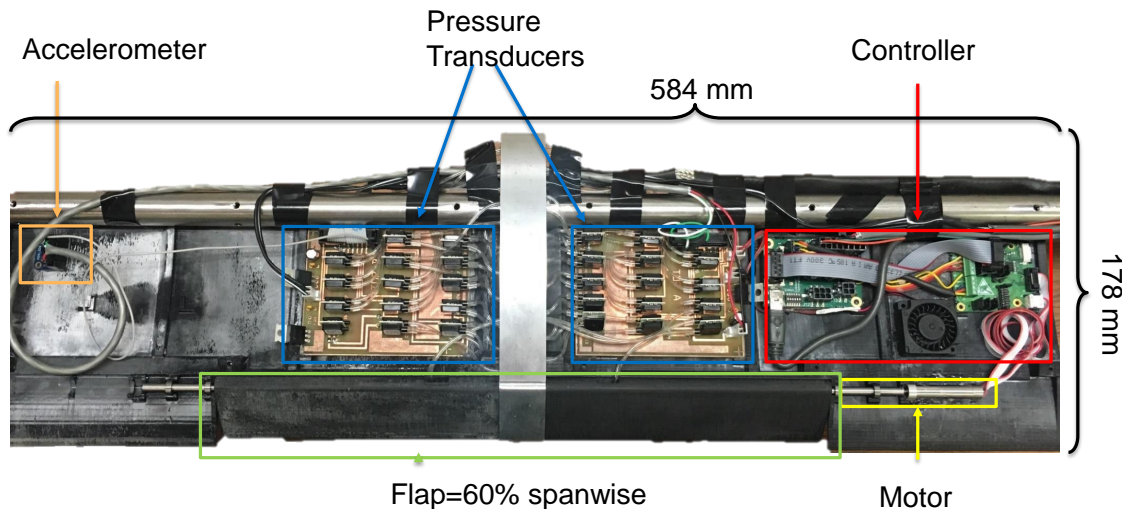

Figure 3. Internal organization of the airfoil showing the sensors used and the TEF actuation system with the airfoil cover removed.

Airfoil Motion

On a rotating wind turbine blade, one mechanism by which the α varies as the blade rotates occurs when the turbine is yawed. Morote (2016) and Burton et al. (2011) modeled the α variation as a function of azimuth position. Gallant and Johnson (2017) compared those previous two models to experimental data on a 3.4 m diameter wind turbine. From the models and experiments it was found that the α variation is very similar to a sine function when the turbine

is yawed. **To simulate the dynamic forces on a yawed wind turbine blade, $\alpha(t)$ follows a sine function as reported by Gharali and Johnson (2015) and described in the following equation:**

$$\alpha\left(t\right) = \alpha_{mean} + \alpha_{amp} sin\left(2\pi f_p t\right) \tag{1}$$

where α_{mean} **is the mean geometric angle of attack of the airfoil,** α_{amp} **is the semi-amplitude for the pitch motion and** f_p **is the airfoil oscillation frequency. To study the influence that the TEF has on the aerodynamic forces on the airfoil, the flap angle oscillation frequency,** f_F**, is the same as the pitch frequency** f_p**. The following equation describes the motion for the flap angle,** $\alpha_F(\mathbf{t})$**:**

$$\alpha_F\left(t\right) = \alpha_{amp,F} sin\left(2\pi f_F t + \phi\right) \tag{2}$$

where $\alpha_{amp,F}$ **is the TEF semi-amplitude and** ϕ **is the phase shift with respect to the pitch motion. Figure 4 shows the positive direction for the pitch and flap angles. There are three airfoil parameters that influence the dynamic stall or unsteady loading: airfoil shape, mean pitching angle/amplitude, and the reduced frequency** $k = \pi c f / U_\infty$ **(**c **is the chord,** f **is the frequency where it is equal to** f_p **in this experimental setup and** U_∞ **is the freestream velocity) (Carr et al., 1977; McCroskey, 1982).**

Corke and Thomas (2015) defined the flow field to be unsteady when k is higher than 0.06 otherwise unsteady effects can be neglected. The system in this study is operated at two different k values of 0.06 and 0.1 to represent the α variation at two different spanwise r/R (where r is the radius of a point on the blade and R is the blade tip radius) locations on a yawed wind turbine blade. **The blade element section studied here was subsequently installed on a 3.6 m diameter wind turbine rotating at a speed of 200 rpm and operating at a tip speed ratio of 3.5. On the turbine,** k **decreases when the blade element is moved away from the hub. A** k **value of 0.06 would occur closer to the blade tip (r/R=0.82) while** k**=0.1 would occur closer to the blade center (r/R=0.66). A** k **value of 0.06 and 0.1 would represent a local tip speed ratio of 2.87 and 2.31 respectively. More information about the wind turbine setup could be found in Samara and Johnson (2020b).** The different test cases reported here are shown in Table 1. Test case 1a and 1b represent a reduced frequency of 0.06 and 0.1 respectively while $\alpha_{amp} = 10°$ and $\alpha_{mean} = 20°$. On the other hand, test case 2, represents k=0.1, $\alpha_{amp} = 5°$ and $\alpha_{mean} = 25°$. Conditions for test 1 causes the airfoil to go into deep dynamic stall while allowing the flow over the airfoil to reattach during the cycle. In test 2, the airfoil is oscillating past the static stall angle thus the flow does not reattach during the cycle.
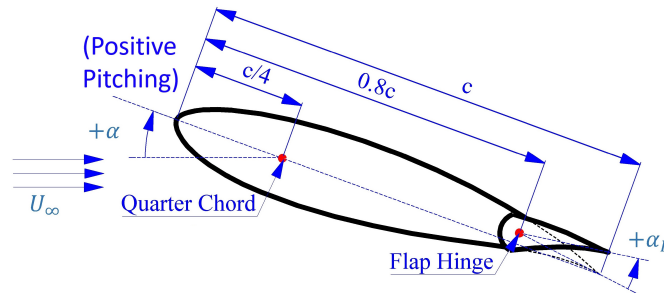

Figure 4. A sketch illustrating the airfoil and flap degrees of freedom. $+\alpha$ positive angle of attack; $+\alpha_F$ positive flap angle; U_∞ freestream velocity

Table 1. Wind tunnel dynamic airfoil oscillation test cases

Test No	f_p (Hz)	k	f_F (Hz)	α_{mean} (°)	α_{amp} (°)	$\alpha_{amp,F}$ (°)	ϕ
Case 1a	1.61	0.06	[0, 1.61]	20	10	20	[0:0.5:1.5] π
Case 1b	2.68	0.1	[0, 2.68]	20	10	20	[0:0.5:1.5] π
Case 2	2.68	0.1	[0, 2.68]	25	5	20	[0:0.5:1.5] π

To better understand the motion of the airfoil and flap with different flap phases, Figure 5 graphically depicts the kinematic motion along with airfoil/flap positions for case 1a or 1b where $\alpha_{mean} = 0°$. The four different flap phases

are plotted along with the airfoil motion schematics at four instances in the cycle. The arrows on the airfoil motion schematic show the direction of motion of the airfoil and flap.
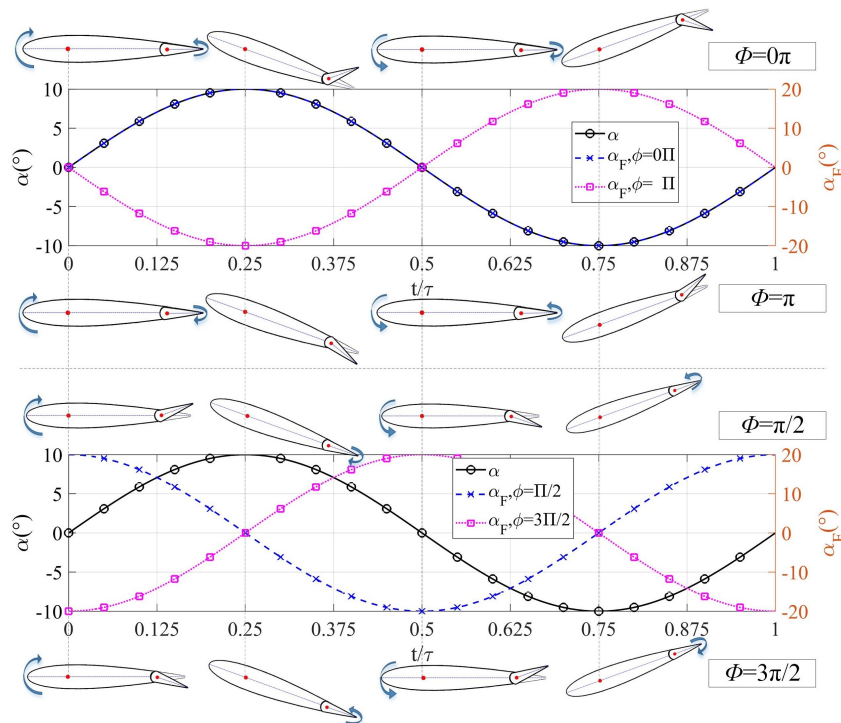

Figure 5. Kinematics of the airfoil and TEF motion for $\alpha_{mean} = 0°$ and different ϕ for case 1a or 1b

Phase-Averaged Cycle Convergence Study

A convergence study was undertaken to ensure the phase-averaged data presented is repeatable, reliable and the number of cycles used is sufficient to represent the averaged cycle-to-cycle variation due to the unsteady nature of the flow. The data presented in Figure 6 show the convergence study on the phase-averaged $C_L - \alpha$ plot and its uncertainty for case 1b where k=0.1 and the airfoil is undergoing deep stall. In this convergence study the phase-averaged data is presented for 5, 10, 50, 100, 200, and 500 cycles. The loop for 5 cycles is only presented to show that even at low cycle number the results are representative of the converged results. Figure 6a also shows repeatability and high confidence in the results and the phase-averaging procedure used to create the plots presented in this paper. The hysteresis loops in Figure 6a start to converge at 100 cycles within 1%. This shows that the use of 200 cycles is sufficient to accurately determine the phase-averaged data for C_L. The C_L uncertainty presented in Figure 6b is the root sum squared of the bias and precision error. Bias error, also known as fixed or systematic error, is mainly due to hysteresis, linearity and temperature shift in the pressure transducers all of which tend to be constant from cycle-to-cycle. Precision error, on the other hand, is dependent on the cycle-to-cycle variation and the number of cycles collected. The two uncertainty in C_L peaks in Figure 6b are then not due to the bias error (because it is constant from cycle-to-cycle) but are due to the precision error as the two peaks represent the motion of the LEVs that tend to be dynamic and unsteady in nature. Most of the cycle-to-cycle variation is likely due to the uncontrolled differences in LEV formation and shedding. Figure 6b also shows very low C_L uncertainty values suggesting high repeatability of the complex flow occurring and that is worth noting. Based on the results presented in this section, at least 500 cycles were used to analyze and produce the subsequent plots.
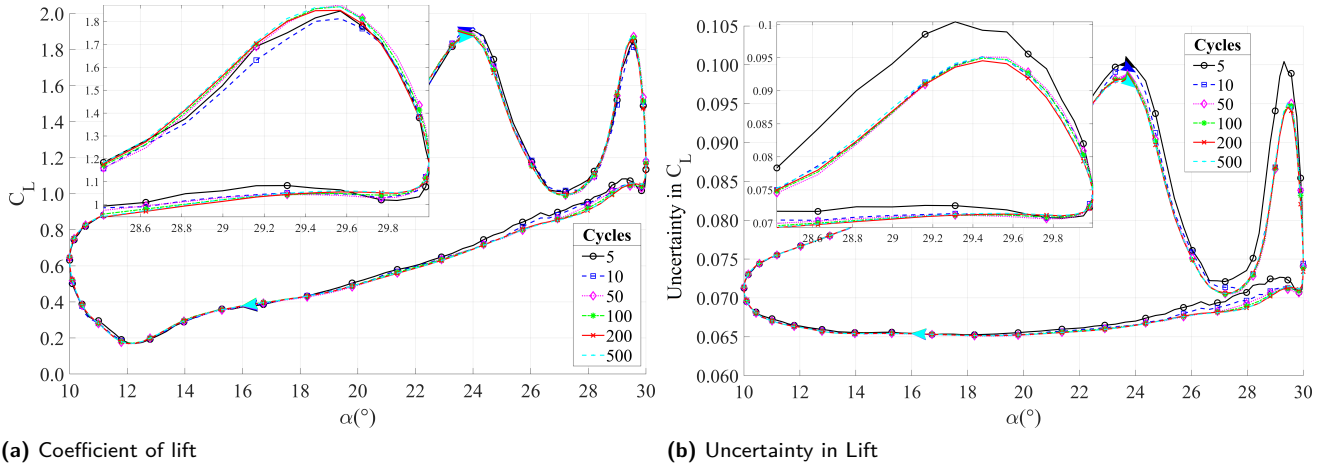
(a) Coefficient of lift

(b) Uncertainty in Lift

Figure 6. A convergence study of the phase-averaged data for different numbers of cycles for a) $C_L - \alpha$ b) Uncertainty in C_L where k=0.1 and $\alpha_{mean} = 20°$ while the flap was fixed. An inset is used to better show the differences between $\alpha = 28.4°$ and $30°$.

Results

Results include a brief description on how large flap angles could influence the aerodynamics of the airfoil by studying the static $C_L - \alpha$, $C_M - \alpha$ and ΔC_p. The second section studies the hysteresis loop while the airfoil is dynamically pitching at two different k values and two α_{mean} angles.

Static Airfoil Characterization

Instead of typically plotting C_L or C_M versus α for the static cases, they are plotted against α_F in Figure 7. Having α_F on the x-axis clearly shows how the TEF influences the lift and moment for a constant α. The static flap angle, α_F, ranged from -40° to 60° in steps of 10° and the pitch angle, α ranged from 0° to 25° in steps of 5°. A more typical lift data versus α for different flap angles could be found in Samara and Johnson (2020a) for the same airfoil. To better understand the C_L data it is important to simultaneously study the contour plots in Figure 8 where ΔC_p is plotted against the chord on the x-axis and α on the y-axis ranging from -40° to 60°. Six individual α cases are plotted ranging from 0° to 25° in steps of 5°. Each contour plot is a matrix of 27 pressure measurements by 11 α_F angles and each point is the average of 4000 data points over a period of 4 seconds. It is imperative then to draw conclusions from both figures (Figures 7 and 8) simultaneously as they complement each other.

Focusing on Figure 7a, as α_F increases (decreasing airfoil camber), C_L decreases as long as $\alpha \leq 10°$ where the flow is attached. When $\alpha = 15°$ the airfoil is operating at the onset of stall but complete flow separation is influenced by α_F because C_L is higher than the $\alpha = 10°$ case for three α_F values and lower for the others. In Figure 8d ($\alpha = 15°$) when $\alpha_F = -40°$ or $-30°$, the flow over the airfoil is completely stalled reducing C_L because the $-\Delta C_p$ peak at the LE is greatly diminished. When $-20 \leq \alpha_F \leq 20°$ the flow is partially attached as evident by the high $-\Delta C_p$ concentration at the LE but not completely attached because C_L is lower than when $\alpha = 10°$. Lastly, for $\alpha_F \geq 30°$ the flow is completely attached as evident by an increase in $-\Delta C_p$ at x/c=0.3 and C_L is higher than when $\alpha = 10°$. For $\alpha = 20°$ and 25°, the trends are similar and could be explained in a similar way. For $\alpha_F \leq 20°$ the flow is completely separated because C_L is reduced and the $-\Delta C_p$ peak at the LE is also greatly diminished as seen in Figures 8e and 8f. When $\alpha_F > 20°$ C_L increases instead of decreasing as α_F increases. This could be attributed to the fact that as the flap angle becomes more positive the flow starts to partially reattach increasing $-\Delta C_p$ along the entire length of the chord as seen in the contour plots.

The TEF can significantly influence C_L as long as the airfoil is not stalled but even in stalled cases some influence is still present. For example, C_L changed from 1.3 to 0 for $\alpha = 10°$ by just changing the flap angle. The slope of C_L change ($d(C_L)/d(\alpha_F)$) is then 0.13/10° as long as the airfoil is not stalled. This linear slope is similar to what was found by Abbott and Doenhoff (1959). The TEF was capable of reattaching the flow over the airfoil for $\alpha = 15°$ and partially reattaching the flow for $\alpha = 20°$ and 25°. The TEF is also capable of producing much higher C_L values than by just changing α. This was also observed by Abbott and Greenberg (1939) for a different airfoil but they also found that C_D increases significantly for positive flap angles only. The maximum C_L value for any α for an airfoil

with no TEF deflection ($\alpha_F = 0°$) is 0.9 but the highest C_L value with the TEF is 1.3 thus 0.4 higher than with no TEF. It is important to note that even though the airfoil is stalled ($\alpha = 20°$ or $25°$), the TEF still has significant impact on C_L.

In Figure 7b as α_F increases (decreasing airfoil camber) C_M increases except for select cases. From the figure it is seen that the flap angle has a large impact on the C_M values. This could be better explained by investigating the ΔC_p contour plots in Figure 8. The contour plots show that as α_F changes, the center of pressure moves along the airfoil chord. C_M tends to be more sensitive to the pressure center location than the magnitude of pressure on the airfoil surface. For example when ΔC_p is concentrated at the LE this causes the airfoil to pitch nose-up making C_M positive. In contrast, when ΔC_p is concentrated at the TE that causes the airfoil to pitch nose-down making C_M negative. Typically for non-stalled airfoils, positive α_F values decrease $-\Delta C_p$ at the TE and the airfoil is in pitch nose-up leading to a positive C_M. The opposite is true, negative α_F values increase $-\Delta C_p$ at the TE and the airfoil is in pitch nose-down leading to a negative C_M. When $\alpha = 20°$ and $25°$, the slope in the C_M data changes at $\alpha_F = 20°$ because $-\Delta C_p$ increases close to the TE as seen in the contour plots and this is attributed to partial flow reattachment. Changing α_F has a larger impact on C_M when compared to the change in α because the center of pressure does not change with α as was also found by Abbott and Doenhoff (1959). In conclusion the TEF influences the flow dynamics over the airfoil with or without stall manipulating C_L and C_M.
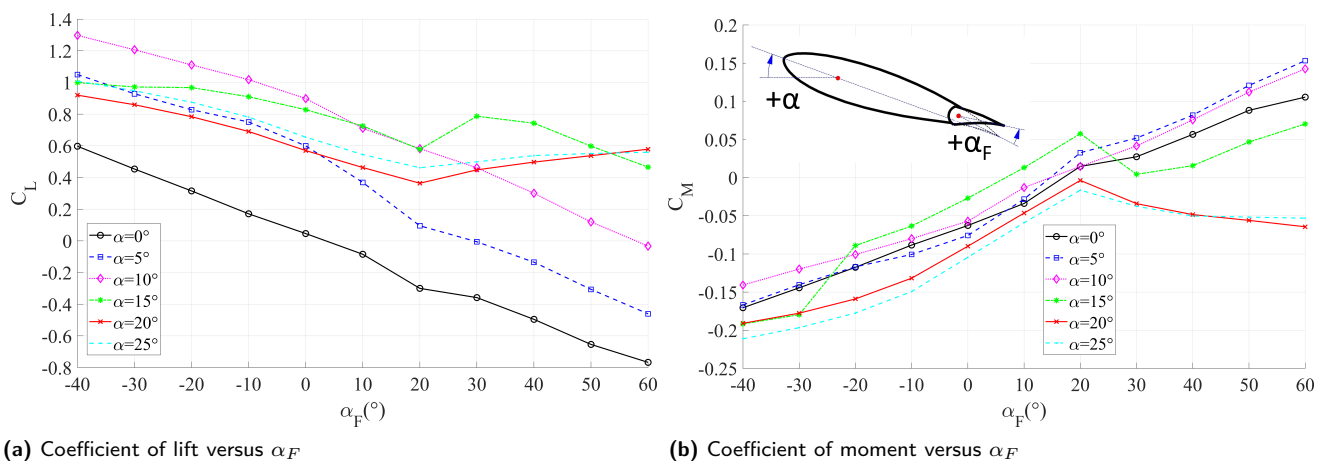

(a) Coefficient of lift versus α_F (b) Coefficient of moment versus α_F

Figure 7. Measured coefficient of lift (C_L) and moment (C_M) versus α_F for several α values

In Figures 8a-c the TEF not only changes ΔC_p close to the TE but also at the LE as well. This indicates how the TEF influences the airflow over the entire chord and not just where the flap is located. In Figure 8d it can be seen that the flow is separated for $\alpha_F = -40°$ and $-30°$ because the $-\Delta C_p$ peak at the LE is absent. Looking at the same plot, at $\alpha_F = 30°$ there is an increase in $-\Delta C_p$ close to the LE and that increased the C_L value in Figure 7a. In Figures 8e-f the trend is similar in both cases and the flow is separated for all α_F. Once the airfoil is stalled then changing the flap angle will not have significant impact on ΔC_p close to the LE but still could impact ΔC_p in the TE region. The isobars in all the plots help show how the TEF impacts ΔC_p. The isobars of $\Delta C_p = 0$ is marked in white dashes to better show negative $-\Delta C_p$ regions. The data and patterns in the contour plots are similar to what was found by Jacobs and Pinkerton (1931) on a RAF 30 airfoil.

Dynamic Pitching

In this section the dynamic pitching and flapping results are presented. The motion of the airfoil and flap are governed by Equations (1) and (2) and the parameters are presented in Table 1. A discussion and detailed analysis regarding the two different cases where α_{mean} is $20°$ and $25°$ are presented. The reason these cases were chosen is explained later in the discussion.

$\alpha_{mean} = 20°$
The data presented in Figures 9 to 14 belong to cases 1a and 1b where $k = 0.06$ and 0.1 respectively with $\alpha_{mean} = 20°$ and $\alpha_{amp} = 10°$. The latter parameters were chosen so the airfoil is operating in deep dynamic stall and around the static stall angle so the flow has the opportunity to reattach on the airfoil. This way the airfoil is oscillating around
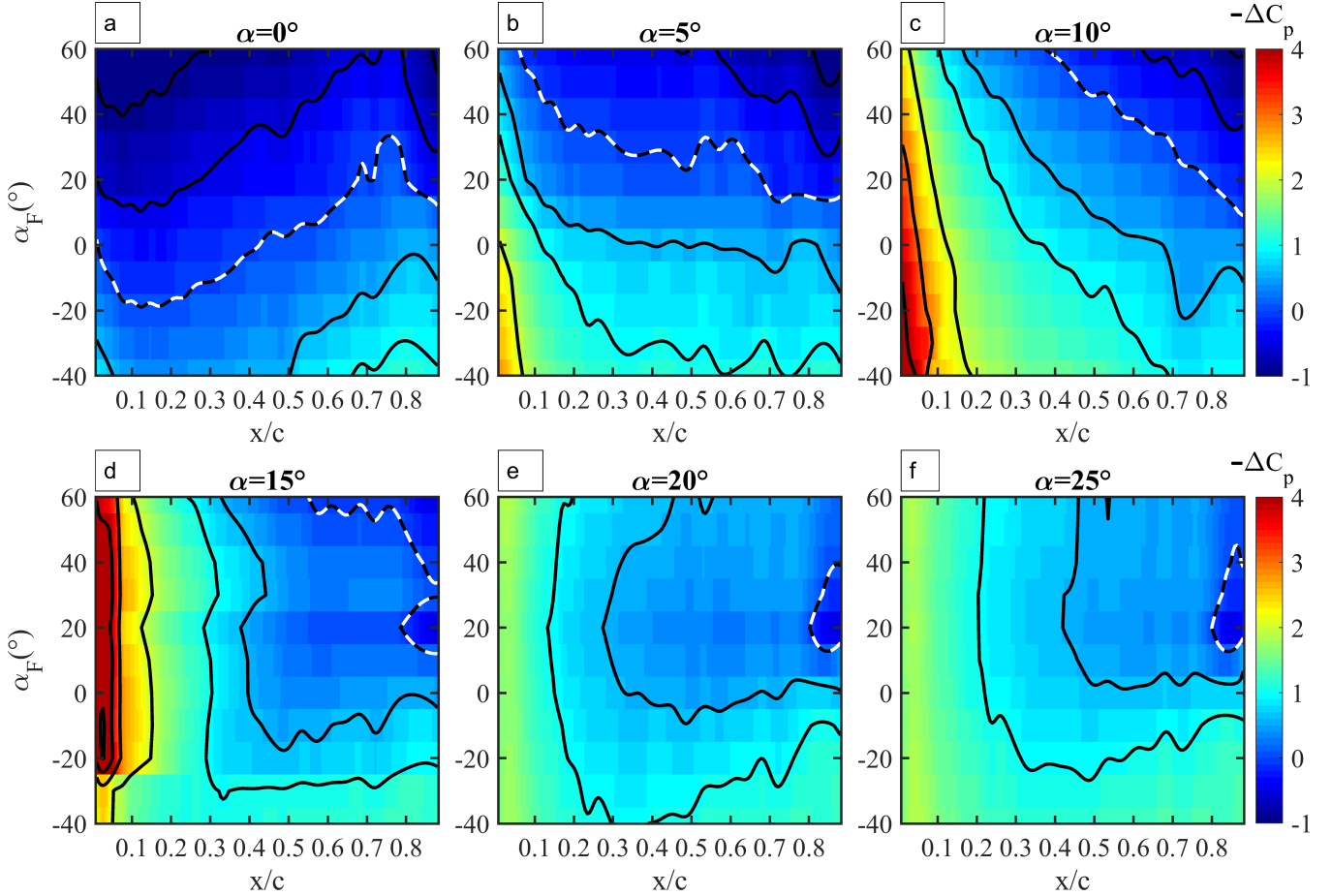
Figure 8. Contours of $-\Delta C_p$ versus x/c versus α_F. a) $\alpha = 0°$, b) $\alpha = 5°$, c) $\alpha = 10°$, d) $\alpha = 15°$, e) $\alpha = 20°$ and f) $\alpha = 25°$. The isobars on the plot represent constant $-\Delta C_p$ values=[-1, -0.5, 0, 0.5, 1, 2, 3, 4]. The isobars of $\Delta C_p=0$ is marked in white dashes.

the static stall angle which is around 16°. Approximately 600 cycles were collected for each scenario and each cycle was binned into 160 equal bins based on cycle period. C_L and C_M are presented in Figure 9 against α for the phase-averaged cycle. The arrows on the plot indicate the direction of motion. The "FixedFlap" case represents a pitching airfoil where the flap is not moving relative to the airfoil. Four equally spaced phase shifts between the pitch and the flap motion denoted by ϕ in Equation (2) are presented.

The C_L phase-averaged loops are presented in two plots, Figures 9a and 9c, where each plot contains a FixedFlap loop, static airfoil data, and 2 flap phases (first: $\phi = 0\pi$ and $\pi/2$, second: $\phi = \pi$ and $3\pi/2$). The static lift data (red stars) is added for comparison. During dynamic stall, C_L is much higher than the static lift data and at certain pitch angles more than twice as much. A similar trend could be seen across the different flap phases but with a slightly different magnitude and location. Starting at $\alpha = 10°$ as the airfoil pitches up, C_L starts to increase but then around $\alpha = 21°$ there is a sudden increase in C_L caused by the primary LEV. After the LEV convects off the airfoil, the flow is separated. Then around $\alpha = 26°$ there is a second sharp increase in C_L this time it is due to a secondary LEV which tends to be weaker in magnitude. The secondary LEV is followed by a subsequent small LEV before the downstroke portion of the cycle. The formation of multiple LEVs is in agreement with past experimental studies and numerical models (Leishman, 1990; Gharali and Johnson, 2013; Zanotti and Gibertini, 2013). It is interesting to note that all the LEV occur during the upstroke only as seen by McCroskey (1981). This could be attributed to the low k value of 0.06 and high α_{mean} of 20°. During downstroke, the airfoil is stalled and C_L keeps decreasing until around $\alpha = 14°$ where the flow starts to reattach and C_L starts to increase. It is interesting to note that C_L is higher than the static points even during the downstroke cycle where the airfoil is stalled and this is due to the nature of dynamic stall. Comparing $\phi = 3\pi/2$ to the FixedFlap, the primary and secondary LEV (which is seen by a spike in

the $C_L - \alpha$ plots) occur 1° earlier while for $\phi = \pi/2$ the LEV occurs 1° later. In the other two ϕ cases (0π and π), the LEV location does not change. Out of all the different ϕ tested it could be concluded that when $\phi = \pi/2$, C_L has the least fluctuation. This is because most of the high peak loads occur halfway through the upstroke portion of the cycle where $\alpha = 20°$. For $\phi = \pi/2$, the magnitude of the C_L peaks caused by the LEV are smaller than the other cases and the hysteresis cycle is narrow. To better understand the kinematics of the pitch and flap motion and the phase offset between the two, refer to Figure 5.
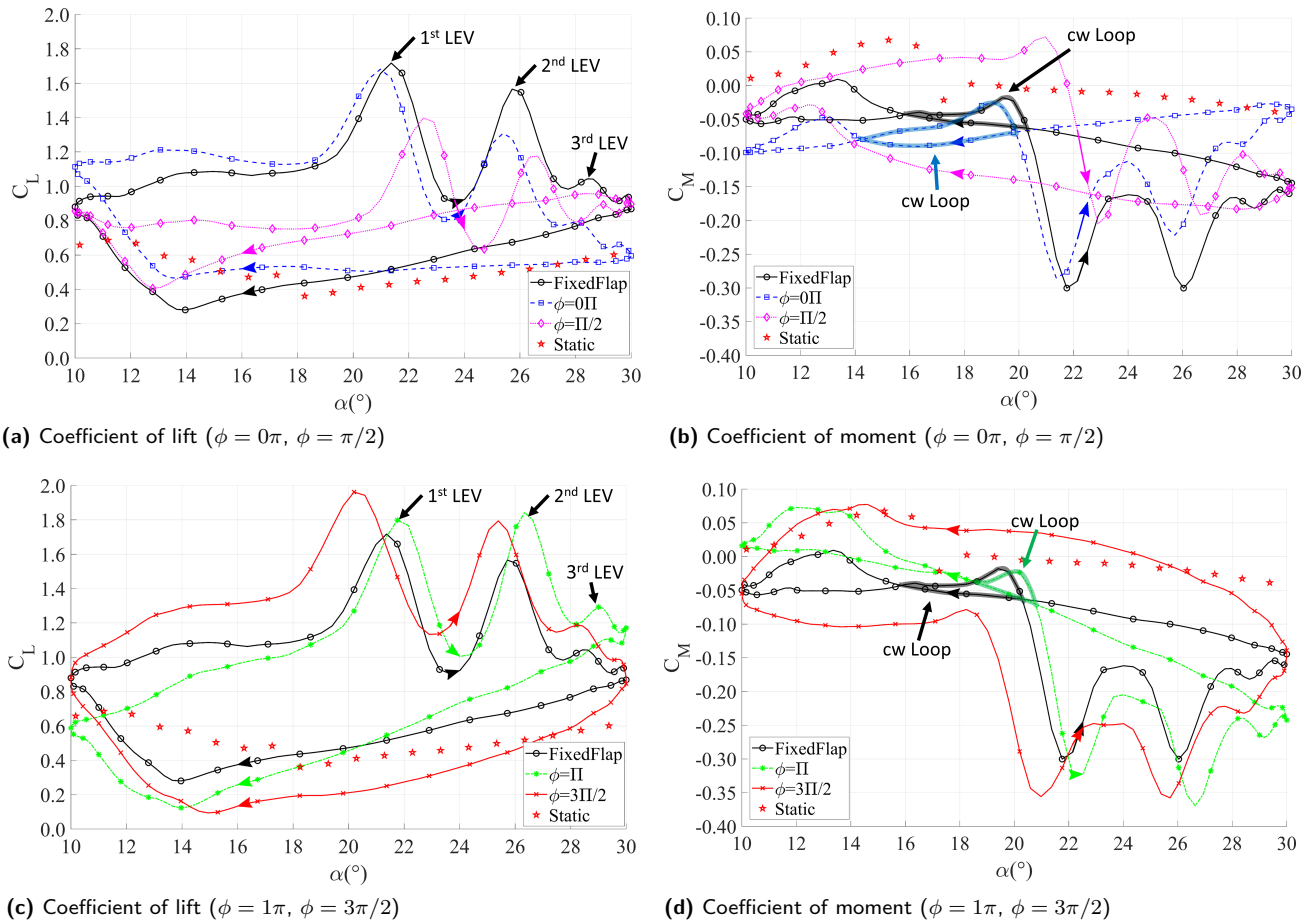

Figure 9. Coefficient of lift (C_L), and moment (C_M) versus α for different flap phases (ϕ) for case 1a where k=0.06 and $\alpha_{mean} = 20°$. Only every 4th data point is shown for clarity. The 1st and 2nd LEV and the cw loops are marked in each plot.

Figures 9b and 9d show the C_M hysteresis loops for case 1a. During dynamic stall the LEV starts from the LE and sweeps towards the TE. While the vortex sweeps over the airfoil, it produces a rapid aft movement of the center of pressure from the LE towards the TE resulting in a large nose-down pitching moment on the airfoil (Leishman, 2006). When the LEV is at the LE it increases C_L but when the LEV is shed towards the TE it increases the C_M value. This is why the peak in C_M always occurs after the peak in C_L for all cases. C_M is in constant nose-down pitching (negative C_M value) for the different ϕ cases when compared to the static values. This indicates that the center of pressure is always behind the quarter-chord of the airfoil towards the TE. Another important point to notice in the C_M loop is the formation of a clockwise (cw) loop that indicates negative damping. A small cw loop is found in the FixedFlap, $\phi = 0\pi$, and $\phi = \pi$ around $\alpha = 18°$. For $\phi = \pi/2$, the entire loop is cw promoting stall flutter while the entire loop for $\phi = 3\pi/2$ is counter-clockwise (ccw) preventing stall flutter at all times. As discussed in the introduction, negative damping promotes flutter and instabilities that lead to severe vibration and mechanical failure if the structural dynamics permit and would be best avoided at all times (Corke and Thomas, 2015). In this experimental setup when negative damping was present, the airfoil section was observed to experience excessive vibration.

Figure 10 represents C_L and C_M for case 1b where k increased from 0.06 to 0.1 and $\alpha_{mean} = 20°$. Focusing on the C_L data there are few major differences when k increases. First, the amplitude of the C_L peaks caused by the LEV are increased and the occurrence of the LEV is delayed by 3°. The primary LEV occurs around 24° followed by a secondary LEV at 29°. This delay in occurrence of the LEV is mainly due to the increase in k that tends to delay dynamic stall to a higher α value (Corke and Thomas, 2015; Leishman, 1990). The secondary LEV again tends to be weaker than the primary LEV. There is also a very small subsequent LEV occurring during the first part of the downstroke cycle. The difference between the upstroke and downstroke increases, widening the hysteresis loop and increasing cyclic loading when k increases. These differences mentioned are in agreement with prior studies (Leishman, 2006; Lee and Gerontakos, 2004; McCroskey, 1981). The loss of lift after the secondary LEV is much steeper and sudden when compared to the k=0.06 case because the secondary LEV occurs when the airfoil is about to change pitch direction at $\alpha = 30°$. From cases 1a and 1b, it is concluded from the C_L loops that for $\phi = \pi/2$ the load fluctuation is smallest, the hysteresis loops are much narrower and the peaks due to the LEV are less severe. On the other hand, $\phi = 3\pi/2$ has the largest load fluctuations, the widest hysteresis loops and the highest peaks.
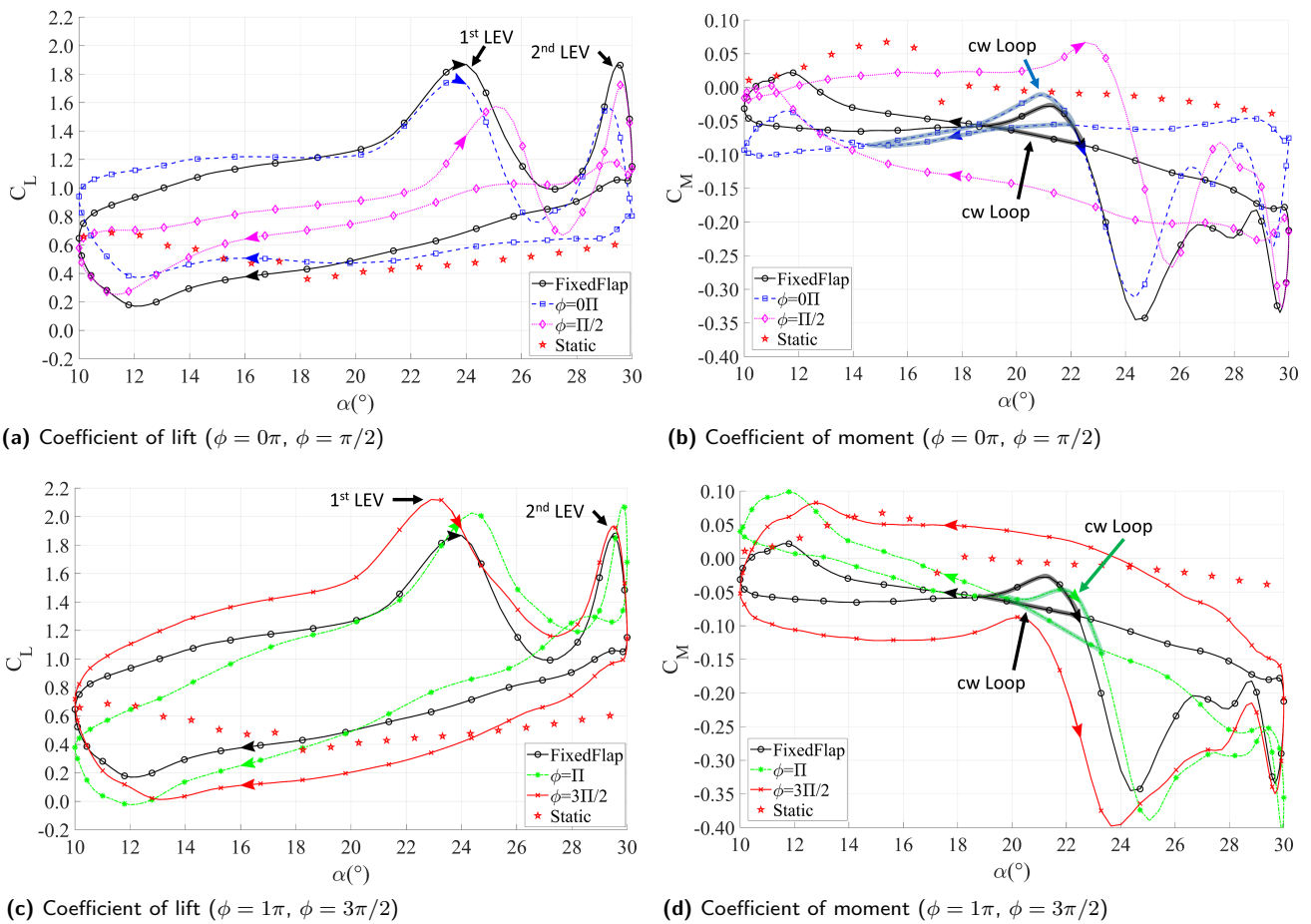

(a) Coefficient of lift ($\phi = 0\pi$, $\phi = \pi/2$)

(b) Coefficient of moment ($\phi = 0\pi$, $\phi = \pi/2$)

(c) Coefficient of lift ($\phi = 1\pi$, $\phi = 3\pi/2$)

(d) Coefficient of moment ($\phi = 1\pi$, $\phi = 3\pi/2$)

Figure 10. Coefficient of lift (C_L), and moment (C_M) versus α for different flap phases (ϕ) for case 1b where k=0.1 and $\alpha_{mean} = 20°$. Only every 4th data point is shown for clarity. The 1st and 2nd LEV and the cw loops are marked in each plot.

Looking at the C_M hysteresis plots in Figure 10 and comparing them to Figure 9 where k increased from 0.06 to 0.1 a few differences arise. C_M peaks are increased and the LEV formation is delayed as seen in the C_L plots. The cw loops now occur around $\alpha = 21°$ instead of 18°. The magnitude of negative damping is about the same. A similar conclusion to that made for the C_L loops is made for the C_M loops, $\phi = \pi/2$ produces the least fluctuations and $\phi = 3\pi/2$ produces the highest fluctuations. On the other hand, $\phi = \pi/2$ leads to a negatively damped C_M loop promoting flutter while $\phi = 3\pi/2$ leads to positive damping. To conclude which ϕ to use to minimize dynamic stall on the airfoil, $\phi = \pi/2$ greatly reduces C_L but at the same time leads to negative damping. Another option is $\phi = 0\pi$

and that reduces C_L peaks slightly but eliminates negative damping. So depending whether to reduce C_L peaks or eliminate negative damping, ϕ should be $\pi/2$ or 0π.

Plotting C_L and C_M versus α is helpful to see the overall trends in the data. **To better understand how the pressure center and magnitude changes over the airfoil surface, a contour plot is used to plot ΔC_p versus airfoil chord on the x-axis (x/c) versus averaged cycle period, t/τ (where t is time and τ is the motion cycle period), on the y-axis. Arrows along the y-axis indicate the direction of airfoil motion, whether it would be upstroke or downstroke. The cycle period, t/τ, could also be associated with α as shown on the right y-axis and the relationship is plotted in Figure 11d for $\phi = 0\pi$. The plots are constructed from a matrix of 27 differential pressure measurements along the airfoil chord by 160 bins representing one complete cycle.** Each point in the matrix is the average of 4000 data points. Figure 11 shows the ΔC_p contour plots for case 1b for FixedFlap, $\phi = \pi/2$, and $\phi = 3\pi/2$ cases. The contour plots for case 1a are not be presented because the plots are very similar to those of case 1b. The pattern for all three ϕ cases presented is similar other than small magnitude and location differences and could be described at the same time. Starting at $t/\tau = 0$, $-\Delta C_p$ is concentrated at the LE (x/c<0.25) and starts to increase until it reaches its highest point at $t/\tau \approx 0.25$ indicating that the flow is attached. After this point the LEV starts to shed from the LE to the TE. As the LEV is shed it tends to decrease $-\Delta C_p$ close to the LE but increases $-\Delta C_p$ on the rest of the airfoil surface. This increase in $-\Delta C_p$ over the airfoil creates the sudden peak in C_L and C_M as seen in Figures 9 and 10. After the primary LEV, $-\Delta C_p$ along the entire airfoil chord is diminished indicating stall until the secondary LEV is formed at $t/\tau \approx 0.45$ but with a weaker magnitude. After the secondary LEV, $-\Delta C_p$ along the entire airfoil chord is diminished again for the rest of the cycle indicating stall. This phase-averaged pattern in ΔC_p for the pitching cycle and how it shows both LEV was also seen experimentally by Zanotti (2012) and Zanotti and Gibertini (2013) for a NACA 23012 airfoil without a TEF. Comparing the three different ϕ cases, the magnitude of the LEV is increased for $\phi = 3\pi/2$ and decreased for the $\phi = \pi/2$ when compared to the FixedFlap as seen more clearly through the isobars on the plots. This comparison was also made by Lee and Su (2011) from the time history of ΔC_p. This concludes that the TEF is not capable of eliminating the LEV formation that causes spikes in the $C_L - \alpha$ and ΔC_p plots but it could reduce its impact on the airfoil.

A different approach to visualize the airfoil stall and the vortex structures can be seen by looking at the standard deviation (STD) in ΔC_p which is plotted in Figure 12 for case 1b. The STD is plotted in log scale to show the small changes at lower values. **Stall and LEVs are typically associated with high pressure fluctuations because of the flow dynamics as reported by Leishman (2006) and these could also be seen in Figure 6 which shows the largest fluctuations occur when the LEV detaches**. While 0<t/τ<0.25 and for all the cases presented, STD(ΔC_p) values are low indicating that the airfoil is not stalled. The primary and secondary LEV discussed in Figure 11 also appear in this figure and are associated with very high STD values at $t/\tau \approx 0.25$ and $t/\tau \approx 0.45$. The time history of the STD(ΔC_p) clearly shows that the movement of the LEV is from the LE to the TE. The observations made here reinforce the discussion made earlier while discussing $C_L - \alpha$ and ΔC_p plots. After both vortices flow past the TE, STD is reduced but still much higher than at $t/\tau = 0$ indicating that the flow over the airfoil is stalled between t/τ=0.5 and 1. The STD is then reduced further at $t/\tau = 0$ when the airfoil starts to pitch upwards indicating flow reattachment. This statement is confirmed in the $C_L - \alpha$ plot in Figure 10 showing that during the downstroke cycle, C_L is much lower than the upstroke cycle until the very end of the cycle. The STD(ΔC_p) patterns do not change significantly between the four ϕ cases presented in the figure other than a slight change in magnitude and location of the peaks.

So far $C_L - \alpha$, $C_M - \alpha$, ΔC_p, and STD(ΔC_p) have been discussed showing the complexity and behavior of dynamic stall but they do not clearly show with absolute certainty which ϕ case reduces the load fluctuations the most. To simply and effectively measure the impact of a TEF on an oscillating airfoil undergoing dynamic stall, a fast Fourier transform (FFT) was performed on the time resolved C_L and root bending moment data separately. The frequency analysis plots are presented in Figure 13 for case 1a. The power spectral density (PSD) on the y-axis was normalized with respect to the peak amplitude found in the FixedFlap case. Frequency on the x-axis was normalized with respect to the oscillation frequency (f_p) and thus the highest amplitude occurs at frequency/f_p =1. There is another peak present at frequency/f_p =2 representing the second harmonic of the oscillation. Both axes of the plot are in log scale to better show the frequency and amplitude distribution and an inset is used to magnify the results around f_p. The plots show that for $\phi = \pi/2$, the C_L peak amplitude at f_p is reduced by 53% while the root bending moment amplitude is reduced by 37% with respect to the FixedFlap case. This reduction is significant and shows that the TEF is capable of reducing cyclic loading. There is a greater measured reduction in C_L than root bending moment
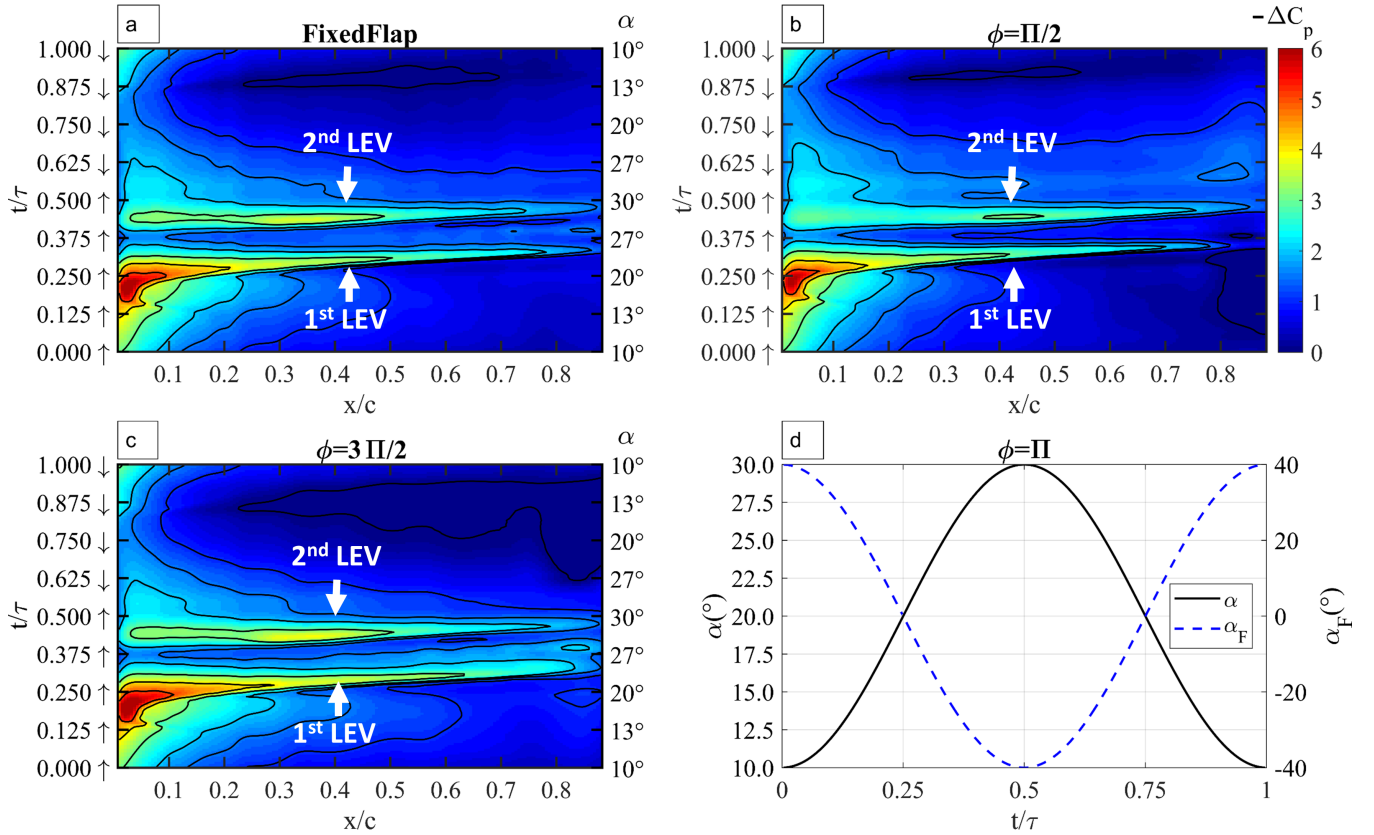
Figure 11. Contours of $-\Delta C_p$ versus x/c versus t/τ for case 1b (k=0.1 and $\alpha_{mean} = 20°$). **a)**, **b)**, and **c)** represent FixedFlap, $\phi = \pi/2$, and $\phi = 3\pi/2$ respectively. **d)** α versus pitch period (t/τ), and flap angle (α_F) for phase $\phi = 1\pi$. The isobars on the plot represent constant $-\Delta C_p$ values=[0, 1, 1.5, 2, 3, 4, 5].

because C_L is measured at the center of the TEF section while the root bending moment measures the lift force for the entire airfoil section where the TEF occupies 60% of the airfoil section.

The PSD is also plotted for case 1b in Figure 14. Comparing case 1b to 1a and for $\phi = \pi/2$, the C_L amplitude is reduced by 26% compared to 53% while the root bending moment amplitude is reduced by 24% compared to 37%. The change in % reduction occurs because higher k values produce larger peaks in the $C_L - \alpha$ plots and the TEF influence over the latter variable is the same independent of k.

$\alpha_{mean} = 25°$

The results published by Gallant and Johnson (2017) indicate that when an operating wind turbine is yawed, the mean oscillating α could be 25° while the amplitude could be 5° under certain conditions. Case 2 in this paper aims to simulate a wind turbine blade under the same conditions mentioned in Gallant and Johnson. Figure 15 shows $C_L - \alpha$ and $C_M - \alpha$ for case 2 and for different ϕ cases where k=0.1, $\alpha_{mean} = 25°$, and $\alpha_{amp} = 5°$. Focusing on the C_L plots (Figures 15a and 15c), the FixedFlap cycle is cw and the hysteresis loop is narrow indicating that the difference between the upstroke and the downstroke motion is minimal. What is most interesting about the different loops is that the airfoil is stalled during the entire cycle but even so, C_L is higher than its static counterpart. There are a few points that indicate that the airfoil is always stalled for all ϕ cases. First, the airfoil motion for case 2 prescribes α to range from 20° to 30° so α is never below the static stall angle thus reattachment does not occur. **Second, the formation of a LEV is not present in any of the loops as there are no sudden peaks in the C_L or C_M plots. The lack of LEV formation indicates that the flow is always separated along the airfoil surface**. Lastly the ΔC_p contour plots presented later in Figure 16 show that $-\Delta C_p$ is never concentrated at the LE and the values are smaller than the static case indicating flow separation. When comparing $\phi = \pi/2$ or $3\pi/2$ to the FixedFlap loop it is found that the C_L loop widens significantly but at the same time C_L does not change
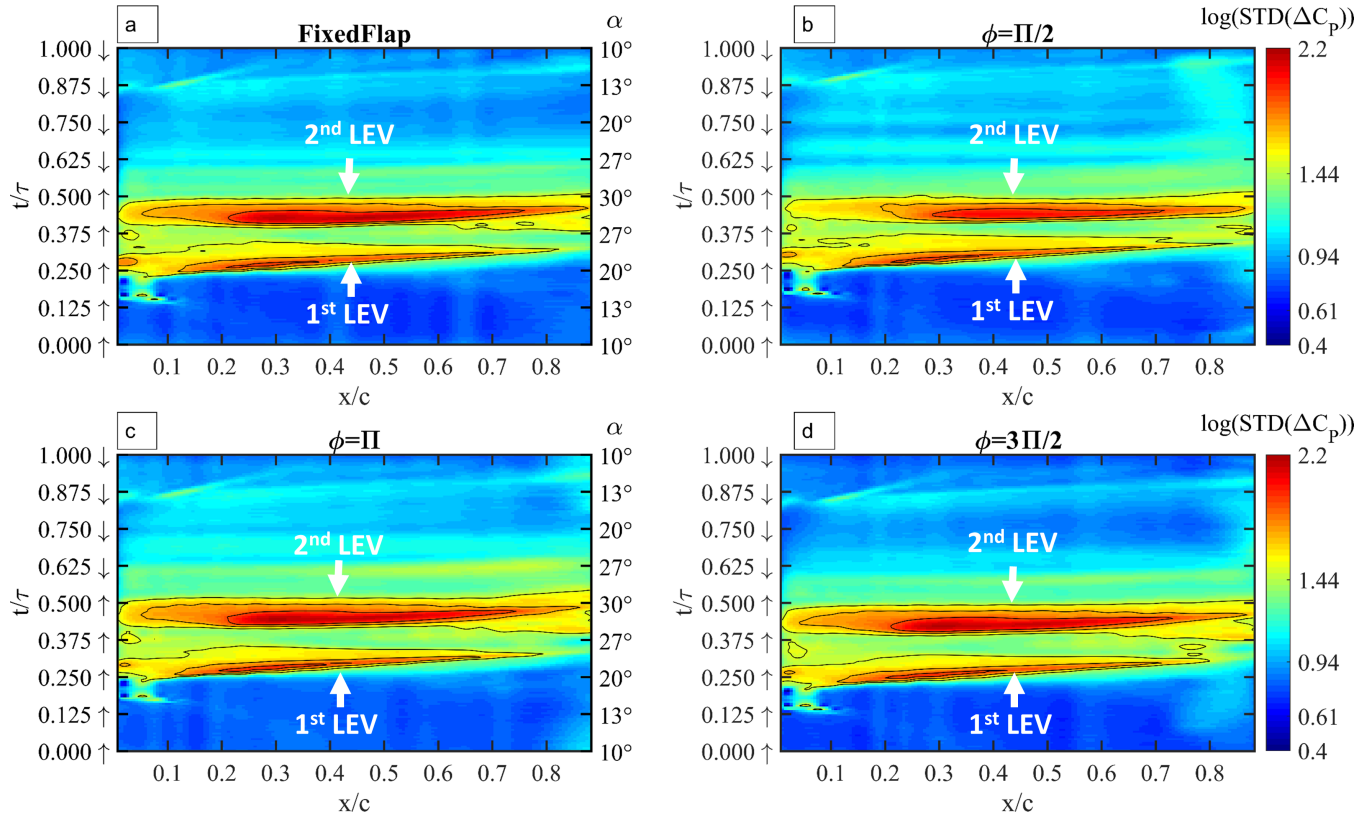
Figure 12. Contour plots showing the STD(ΔC_p) versus x/c versus t/τ for case 1b where k=0.1 and $\alpha_{mean} = 20°$. a), b), c), and d) represent FixedFlap, $\phi = \pi/2$, $\phi = 1\pi$, and $\phi = 3\pi/2$ respectively. The isobars on the plot represent constant log(STD(ΔC_p)) values.
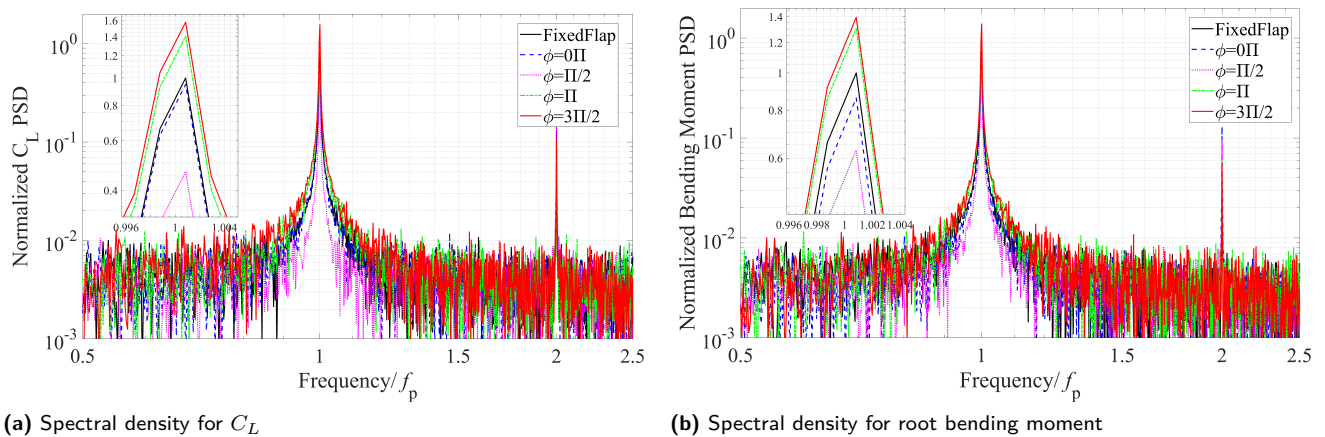

(a) Spectral density for C_L

(b) Spectral density for root bending moment

Figure 13. Normalized power spectral density (PSD) distribution for C_L and root bending moment for different flap phases (ϕ) for case 1a where k=0.06 and $\alpha_{mean} = 20°$. Frequency on the x-axis was normalized with respect to the oscillation frequency (f_p). Both axes are log scale and an inset is shown to magnify the results around f_p.

when α is at its extreme values. On the other hand, when comparing $\phi = 0\pi$ or $\phi = \pi$ to the FixedFlap loop, it was found that the width of the C_L loops does not change and stays narrow but the C_L extreme values are altered when α is at its minimum or maximum value. This shows that the TEF can manipulate C_L at any point on the cycle and

(a) Power spectral density for C_L

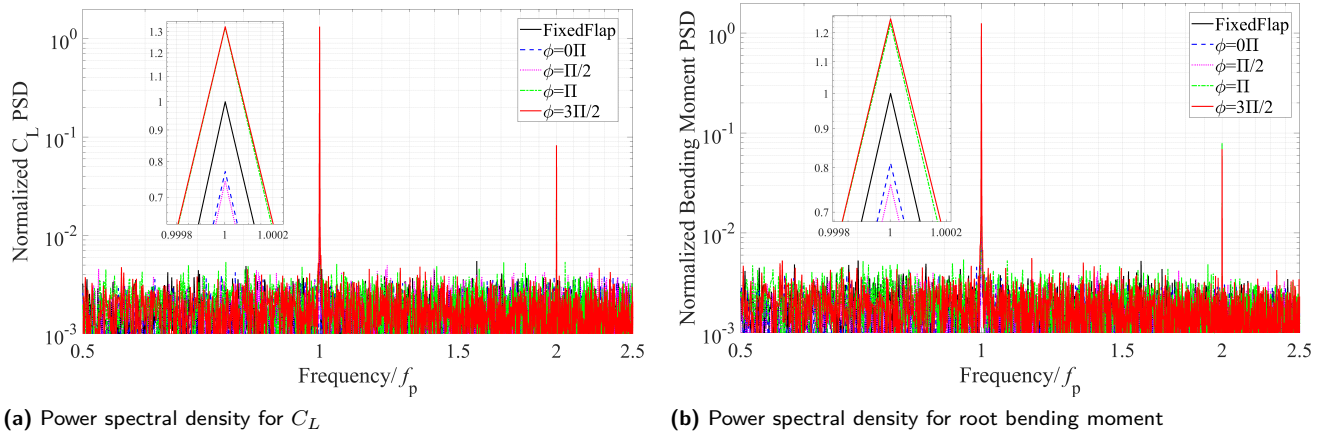**(b)** Power spectral density for root bending moment

Figure 14. Normalized power spectral density (PSD) distribution for C_L, and root bending moment for different flap phases (ϕ) for case 1b where k=0.1 and $\alpha_{mean} = 20°$. Frequency on the x-axis was normalized with respect to the oscillation frequency (f_p). Both axes are log scale and an inset is shown to magnify the results around f_p.

that point is determined by the variable ϕ. To reduce the C_L fluctuation and keep the value constant for the entire cycle then it is recommended to set $\phi = 0\pi$ and reduce $\alpha_{amp,f}$ from $20°$ to approximately $15°$.

Figures 15b and 15d represent C_M versus α for the different ϕ cases. For all cases, C_M is lower than its static counterpart indicating the center of pressure is past the quarter-chord of the airfoil. This is confirmed by the ΔC_p contour plots in Figure 16. In the FixedFlap, $\phi = 0\pi$, and $\phi = \pi$ the C_M loops are narrow and ccw eliminating the possibility of stall flutter. For $\phi = \pi/2$ the C_M loop widens significantly and is cw promoting stall flutter on the airfoil. As for $\phi = 3\pi/2$, the C_M loop is also wide but the loop is ccw eliminating the possibility of stall flutter. To reduce C_M fluctuations and achieve a constant C_M, it is concluded to use $\phi = 0\pi$ but also reduce $\alpha_{amp,f}$ from $20°$ to approximately $15°$. This conclusion is aligned with the one made for the $C_M - \alpha$ loops.

To study how the pressure over the airfoil surface changes in distribution and magnitude, $-\Delta C_p$ versus x/c versus t/τ is plotted in Figure 16 similar to the plots in Figure 11. From the contour plots, it could be noticed that the airfoil is stalled because the $-\Delta C_p$ values are much smaller and less concentrated at the LE when compared to case 1 in Figure 11. This occurs because for case 2, α never goes below the static angle and the flow does not have the opportunity to reattach over the airfoil surface. Case 2 is stalled during the entire cycle despite the fact that it is oscillating between $20° \leq \alpha \leq 30°$ and within the oscillating bound of case 1 where $10° \leq \alpha \leq 30°$ and the flow was attached during part of the case 1 cycle. When comparing $\phi = 0\pi$ to the FixedFlap case a few areas of interest are noted. At $t/\tau = 0.5$, $-\Delta C_p$ close to the TE (x/c>0.75) becomes negative due to the fact that $\alpha_F = 20°$ is creating a lower suction pressure on the suction side. On the other hand, when $t/\tau = 0$ or 1 indicating that $\alpha_F = -20°$, it creates a higher suction pressure on the suction side close to the TE. The opposite is true when $\phi = \pi$, the suction pressure increases at $t/\tau = 0.5$ and decreases at $t/\tau = 0$ and 1 when compared to the FixedFlap case. The TEF did not just have influence on the TE pressure but also on the LE pressure as well as could be seen in the contour plots and the isobars. This indicated that the TEF influences the aerodynamics around the entire airfoil when the flow is stalled or attached.

Conclusions

Initially static measurements of C_L and C_M versus large trailing edge flap (TEF) angles (α_F) were presented for an S833 airfoil installed with a TEF. Changing α_F is capable of producing much higher C_L values than by just changing the pitch angle. The TEF can move the center of pressure on the airfoil surface thus greatly influencing C_M. The ΔC_p contour plots showed that the TEF influences the airflow over the entire chord and not just where the flap is located.

A series of hysteresis loops for C_L and C_M versus angle of attack (α) were presented for a pitching airfoil in deep dynamic stall with reduced frequencies (k) of 0.06 and 0.1. The TEF was oscillating at the same pitching frequency with a constant phase offset, ϕ. It was found that ϕ has a strong impact on the hysteresis loops manipulating the load fluctuations. Due to dynamic stall, the pitching motion created two very noticeable leading edge vortices (LEVs) and
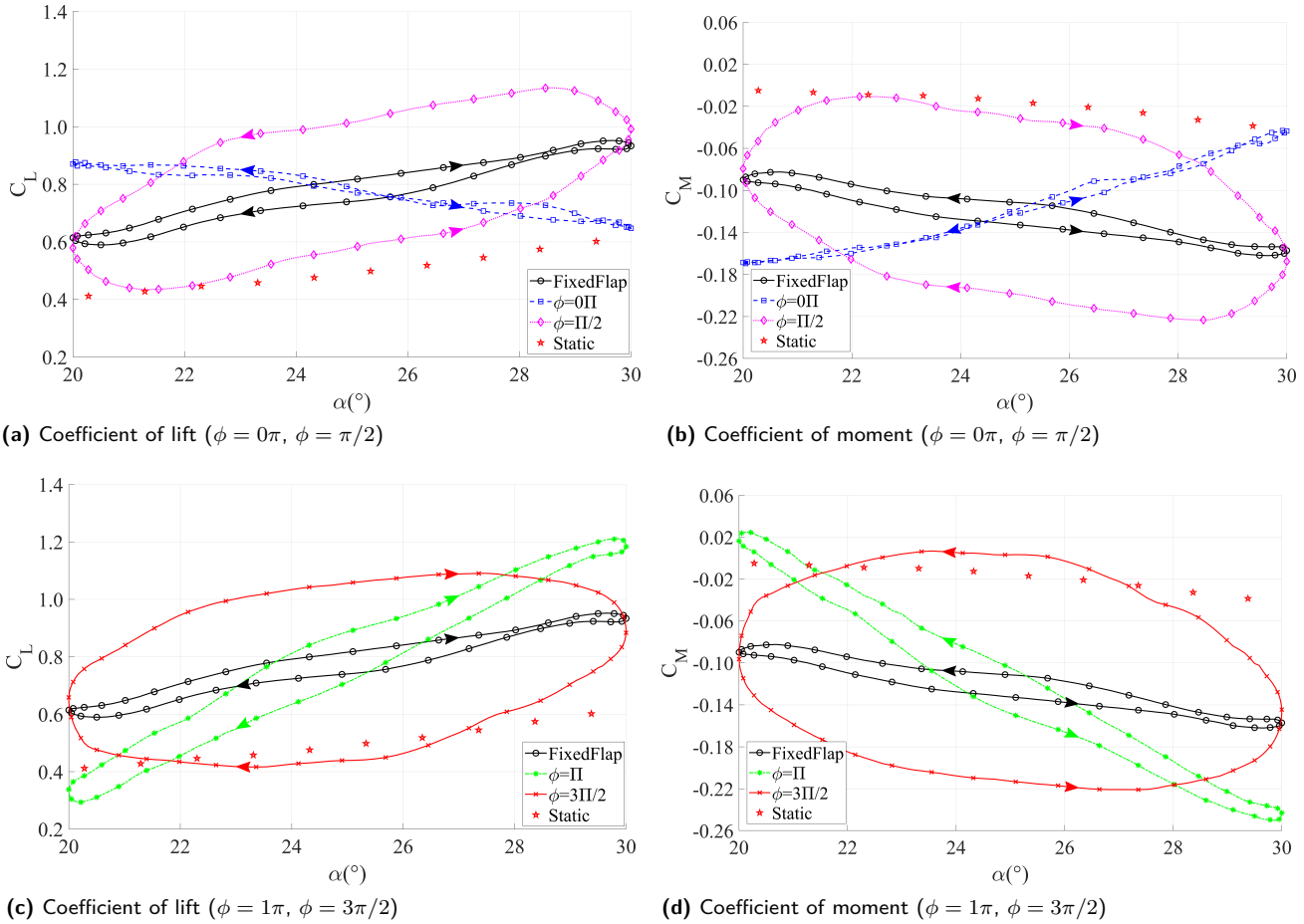
Figure 15. Coefficient of lift (C_L), and moment (C_M) versus α for different flap phases (ϕ) for case 2 where k=0.1, $\alpha_{mean} = 25°$, and $\alpha_{amp} = 5°$. Only every 4th data point is shown for clarity.

minor subsequent LEV where changes in ϕ were responsible for promoting or delaying the occurrence of the LEV in the cycle by 1°. The formation of multiple LEV is in agreement with previous studies. The $C_M - \alpha$ loops showed that as the LEV sweeps over the airfoil, it produces a rapid aft movement of the center of pressure from the leading edge towards the trailing edge resulting in a large nose-down pitching moment on the airfoil. The unique contour plots presented in this paper showed the suction peak locations, the primary and secondary LEV formation and the flow separation on the airfoil. It was found that as the LEV is shed, it tends to decrease $-\Delta C_p$ close the LE but increases $-\Delta C_p$ on the rest of the airfoil surface thus moving the center of pressure.

Two different k values, 0.06 and 0.1, were tested to represent two different spanwise locations on a yawed wind turbine blade. When k increased from 0.06 to 0.1 a few significant differences arose in the hysteresis loops: the amplitude of the C_L peaks caused by LEV are increased and the occurrence of the LEV is delayed by 3°; the difference between the upstroke and downstroke increases, widening the hysteresis loop and increasing load fluctuations; the occurrence of the clockwise loop, that promotes flutter, is delayed by 3° and the magnitude of negative damping is about the same. Out of all the different ϕ tested, it could be concluded that when $\phi = \pi/2$, C_L and C_M have the least fluctuations reducing the magnitude of the peaks caused by the LEV and making the hysteresis loops narrower. Normalized power spectral density (PSD) distribution for C_L and root bending moment were presented to determine with absolute certainty which ϕ case reduces the load fluctuations the most. It was found that for $\phi = \pi/2$, C_L PSD amplitude is reduced by at least 26% while the root bending moment PSD amplitude is reduced by at least 24%. It can be concluded that the TEF is not capable of eliminating the LEV completely but it can reduce its impact on the airfoil.
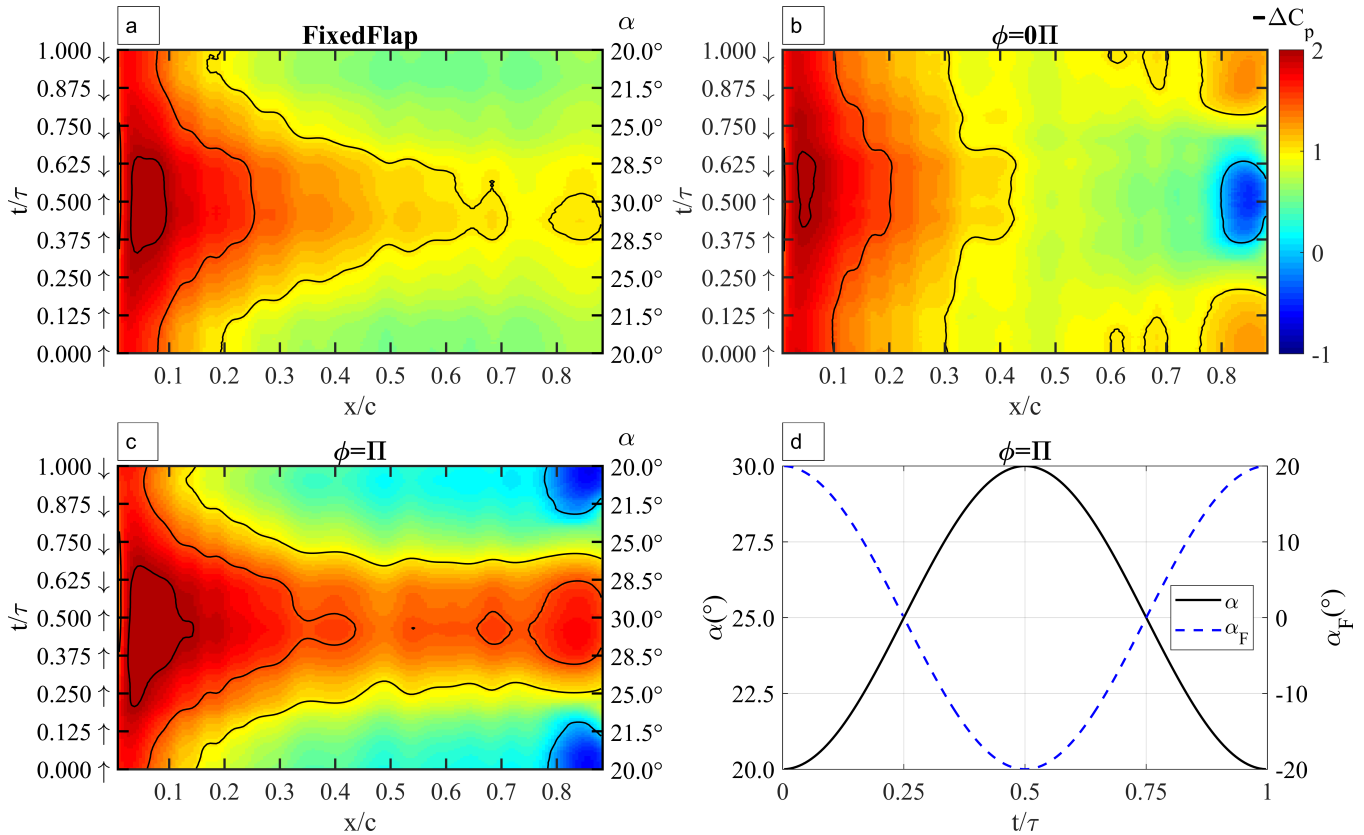
Figure 16. Contour plots showing $-\Delta C_p$ versus x/c versus t/τ for case 2 where k=0.1, $\alpha_{mean} = 25°$ and $\alpha_{amp} = 5°$. a), b), and c) represent FixedFlap, $\phi = 0\pi$, and $\phi = 1\pi$ respectively. d) shows α versus pitch period and flap angle for phase of 1π. The isobars on the plot represent constant ΔC_p values.

Case 2 in this paper is aimed to simulate a wind turbine blade section operating in yawed condition with a pitching amplitude and mean equivalent to what was found in the literature. What was most interesting about the different loops is that the airfoil is stalled during the entire cycle but even so, C_L was higher than its static counterpart. The hysteresis loops for different ϕ cases showed that the TEF can manipulate C_L at any point on the cycle and that point is determined by ϕ.

The data presented throughout this paper will contribute towards continued development of TEF and its influence over the dynamic stall cycle. More experimental data and analysis are needed to determine the influence of a TEF over the dynamic stall cycle for a cambered airfoil. The deep dynamic stall cases presented where the pitch angle reaches 30° are specially unique and novel with important applications to wind turbines and have not been previously reported in the literature. It is anticipated that the discussed experimental data will serve as one of many instruments for gauging, designing, analyzing and optimizing the use of TEF to reduce load fluctuations on wind turbine blades.

Acknowledgements

References

Abbott IH and Doenhoff AEV (1959) *Theory of Wing Sections: Including a Summary of Airfoil Data*. Dover Publication Inc.

Abbott IH and Greenberg H (1939) Tests in the variable-density wind tunnel of the NACA 23012 airfoil with plain and split flaps. *National Advisory Committee for Aeronautics* NACA-TR-66(NACA-TR-661).

Baik YS, Bernal LP, Granlund K and Ol MV (2012) Unsteady force generation and vortex dynamics of pitching and plunging aerofoils. *Journal of Fluid Mechanics* 709: 37–68. DOI:https://doi.org/10.1017/jfm.2012.318.

Barlas TK and van Kuik GAM (2010) Review of state of the art in smart rotor control research for wind turbines. *Progress in Aerospace Sciences* 46(1): 1–27. DOI:https://doi.org/10.1016/j.paerosci.2009.08.002.

Burton T, Jenkins N, Sharpe D and Bossanyi E (2011) *Wind Energy Handbook*. Second edition. Wiley.

Carr LW, McAlister KW and McCroskey WJ (1977) Analysis of the Development of Dynamic Stall Based on Oscillating Airfoil Experiments. *NASA* TN D-8382: 59–64.

Cebeci T, Platzer M, Chen H, Chang KC and Shao JP (2005) *Analysis of Low-Speed Unsteady Airfoil Flows*. Springer New York. ISBN 3540229329.

Corke TC and Thomas FO (2015) Dynamic Stall in Pitching Airfoils: Aerodynamic Damping and Compressibility Effects. *Annual Review of Fluid Mechanics* 47(1): 479–505. DOI:https://doi.org/10.1146/annurev-fluid-010814-013632.

Dykes K, Veers P and Lantz E (2019) IEA Wind TCP: Results of IEA Wind TCP Workshop on a Grand Vision for Wind Energy Technology. Technical Report April, National Renewable Energy Laboratory (NREL).

Feszty D, Gillies EA and Vezza M (2004) Alleviation of Airfoil Dynamic Stall Moments via Trailing-Edge Flap Flow Control. *AIAA Journal* 42(1): 17–25. DOI:https://doi.org/10.2514/1.853.

Gallant T and Johnson DA (2017) Flow angle measurement of a yawed turbine and comparison to models. *Wind Energy Science Discussions* 2(January): 1–17. DOI:10.5194/wes-2016-57.

Gerontakos P (2004) *An Experimental Investigation of Flow Over an Oscillating Airfoil*. PhD Thesis, McGill University.

Gharali K and Johnson DA (2013) Dynamic stall simulation of a pitching airfoil under unsteady freestream velocity. *Journal of Fluids and Structures* 42: 228–244. DOI:https://doi.org/10.1016/j.jfluidstructs.2013.05.005.

Gharali K and Johnson DA (2015) Effects of nonuniform incident velocity on a dynamic wind turbine airfoil. *Wind Energy* 18(2): 237–251. DOI:https://doi.org/10.1002/we.1694.

Gharali Kb, Johnson D, Lam V and Gu M (2015) A 2D blade element study of a wind turbine rotor under yaw loads. *Wind Engineering* 39(5): 557–568. DOI:10.1260/0309-524X.39.5.557.

Green R, Gillies E and Wang Y (2011) Trailing edge flap flow control for dynamic stall. *Aeronautical Journal* 115(1170): 493–503. DOI:https://doi.org/10.1017/S0001924000006138.

Houghton E and Carpenter P (2002) *Aerodynamics for Engineering Students*. Fifth edition. Butterworth Heinemann.

Jacobs EN and Pinkerton RM (1931) Pressure Distribution Over a Symmetrical Airfoil Section with Trailing Edge Flap. *National Advisory Committee for Aeronautics* (Report No. 360).

Lee T and Gerontakos P (2004) Investigation of flow over an oscillating airfoil. *Journal of Fluid Mechanics* 512: 313–341. DOI:https://doi.org/10.1017/S0022112004009851.

Lee T and Gerontakos P (2006) Dynamic Stall Flow Control via a Trailing-Edge Flap. *AIAA Journal* 44(3): 469–480. DOI: https://doi.org/10.2514/1.17263.

Lee T and Su YY (2011) Unsteady airfoil with a harmonically deflected trailing-edge flap. *Journal of Fluids and Structures* 27(8): 1411–1424. DOI:https://doi.org/10.1016/j.jfluidstructs.2011.06.008.

Leishman JG (1990) Dynamic stall experiments on the NACA 23012 aerofoil. *Experiments in Fluids* 9(1-2): 49–58. DOI: https://doi.org/10.1007/BF00575335.

Leishman JG (2006) *Principles of Helicopter Aerodynamics*. Second edition. Cambridge University Press.

Masdari M, Seyednia M and Tabrizian A (2018) An experimental loading study of a pitching wind turbine airfoil in near- and post-stall regions. *Journal of Mechanical Science and Technology* 32(8): 3699–3706. DOI:https://doi.org/10.1007/s12206-018-0722-7.

McCroskey WJ (1981) The Phenomenon of Dynamic Stall. *DTIC Document NASA* .

McCroskey WJ (1982) Unsteady Airfoils. *Annual Review of Fluid Mechanics* 14:285-311: 285–311. DOI:https://doi.org/10.1146/annurev.fl.14.010182.001441.

McCroskey WJ, Carr LW and McAlister KW (1976) Dynamic Stall Experiments on Oscillating Airfoils. *AIAA Journal* 14(1): 57–63. DOI:https://doi.org/10.2514/3.61332.

Morote J (2016) Angle of attack distribution on wind turbines in yawed flow. *Wind Energy* 19(4): 681–702. DOI: https://doi.org/10.1002/we.1859.

Pitt Ford CW and Babinsky H (2013) Lift and the leading-edge vortex. *Journal of Fluid Mechanics* 720: 280–313. DOI: https://doi.org/10.1017/jfm.2013.28.

Raiola M, Discetti S, Ianiro A, Samara F, Avallone F and Ragni D (2018) Smart Rotors: Dynamic-Stall Load Control by Means of an Actuated Flap. *AIAA Journal* 56(4): 1–14. DOI:https://doi.org/10.2514/1.J056342.

Samara F (2020) *Active Aerodynamic Modification of Wind Turbine Blades to Reduce Load Fluctuation*. Phd thesis, University of Waterloo. URL http://hdl.handle.net/10012/15760.

Samara F and Johnson DA (2018) In-blade Load Sensing on 3D Printed Wind Turbine Blades Using Trailing Edge Flaps. *Journal of Physics* 1037: 052023. DOI:10.1088/1742-6596/1037/5/052023.

Samara F and Johnson DA (2020a) Dynamic Stall on Pitching Cambered Airfoil with Phase Offset Trailing Edge Flap. *AIAA Journal* : 1–13DOI:10.2514/1.J059115.

Samara F and Johnson DA (2020b) In-Blade Measurements of Cyclic Loading on Yawed Turbines with Trailing Edge Flap. *Journal of Physics* 1452(1): 012061. DOI:10.1088/1742-6596/1452/1/012061.

Shehata I, Zakaria MY, Hussein A and Hajj MR (2018) Aerodynamic analysis of flapped airfoil at high angles of attack. *AIAA Aerospace Sciences Meeting, 2018* (210059). DOI:10.2514/6.2018-0037.

Shipley DE, Miller MS, Robinson MC, Luttges MW and Simms DA (1995) Dynamic stall occurrence on a horizontal axis wind turbine blade. Technical Report July, National Renewable Energy Laboratory (NREL), Golden, CO (United States). DOI:10.2172/61151. URL http://www.osti.gov/servlets/purl/61151/.

Somers DM (2005) The S833 , S834 , and S835 Airfoils. *National Renewable Energy Laboratory, NREL* NREL/SR-50. DOI: 10.2172/15020040.

Troldborg N (2005) Computational Study of the Risø-B1-18 Airfoil with a Hinged Flap Providing Variable Trailing Edge Geometry. *Wind Engineering* 29(2): 89–113. DOI:10.1260/0309524054797159. URL http://journals.sagepub.com/doi/10.1260/0309524054797159.

Zanotti A (2012) *Retreating Blade Dynamics Stall*. Phd thesis, Politecnico di Milano.

Zanotti A and Gibertini G (2013) Experimental investigation of the dynamic stall phenomenon on a NACA 23012 oscillating airfoil. *Proceedings of the Institution of Mechanical Engineers, Part G: Journal of Aerospace Engineering* 227(9): 1375–1388. DOI:10.1177/0954410012454100.

Zanotti A and Gibertini G (2018) Experimental assessment of an active L-shaped tab for dynamic stall control. *Journal of Fluids and Structures* 77: 151–169. DOI:10.1016/j.jfluidstructs.2017.11.010.